CFD-DEM study on agglomeration and spout-assisted fluidization of cohesive particles
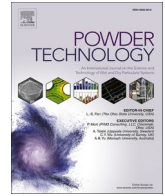
Zou, Yi; Zou, Ruiping; Wu, Yongli

Important note
To cite this publication, please use the final published version (if applicable).
Please check the document version above.

CFD-DEM study on agglomeration and spout-assisted fluidization of cohesive particles

Yi Zou [a], Ruiping Zou [b], Yongli Wu [c,*]

[a] Southeast University-Monash University Joint Research Institute, Suzhou, China
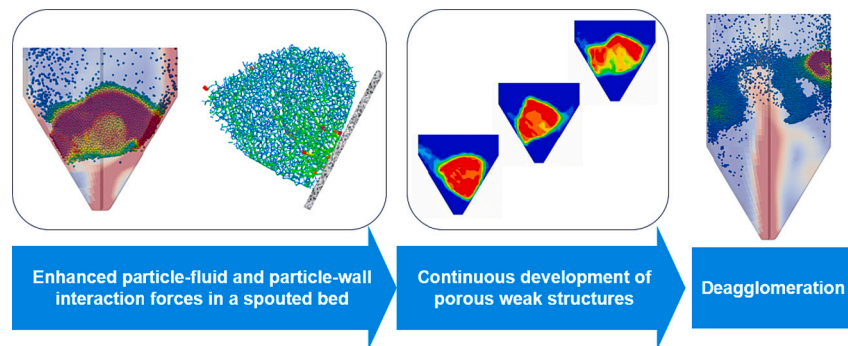[b] ARC Research Hub for Smart Process Design and Control, Department of Chemical and Biological Engineering, Monash University, Clayton, Australia
[c] Faculty of Civil Engineering and Geosciences, Delft University of Technology, Delft, the Netherlands

HIGHLIGHTS

- Effects of particle cohesion on the mixing and agglomeration of particles are analyzed.
- Defluidization of a bed due to large agglomerates is examined.
- The effectiveness of spout-assisted fluidization of cohesive particles is demonstrated.
- Effective design for the conical geometry of a spouted bed is identified.
- Mechanisms underlying spout-assisted deagglomeration and fluidization are explained.

GRAPHICAL ABSTRACT

Enhanced particle-fluid and particle-wall interaction forces in a spouted bed → **Continuous development of porous weak structures** → **Deagglomeration**

ARTICLE INFO

ABSTRACT

The agglomeration of cohesive particles can deteriorate fluidization quality and cause the defluidization of a bed, which is a common issue found in the applications of fluidized beds. This study aims to gain a better understanding of particle cohesion on agglomeration/fluidization behaviors and the effective methods for achieving a better fluidization quality, through numerical simulations based on the coupled approach of computational fluid dynamics and discrete element method (CFD-DEM). The effects of particle cohesion, gas velocities or flow conditions, and the bed geometry on the agglomeration and fluidization behaviors are analyzed. It is shown that the increase of particle cohesion can lead to deteriorated particle mixing, significant agglomeration of particles, and defluidization of the bed; the agglomeration-induced defluidization of highly cohesive particles is difficult to mitigate in a conventional flat-bottom fluidized bed. As large-sized agglomerates are more frequently found in the bottom of the bed, the spouted gas flow is then utilized and demonstrated to be effective in assisting the deagglomeration and fluidization of highly cohesive particles. Through the comparison of various spouted beds and spouted fluidized beds, the effective design of the bed bottom is identified for achieving a higher fluidization quality. Corresponding mechanisms underlying spout-assisted deagglomeration and fluidization are found to be much related to not only the enhanced particle-fluid but also particle-wall interactions in the confined space of a conical bed bottom, thus explaining the effectiveness and the importance of the bottom conical geometry of

* Corresponding author.
E-mail address: y.wu-7@tudelft.nl (Y. Wu).

spouted beds. The obtained findings may help to understand the agglomeration-induced defluidization of fluidized beds and assist the fluidization of highly cohesive particles by the effective design of spouted beds.

1. Introduction

The fluidization of cohesive particles like fine powders (e.g., Group A and C powders) and wet particles is widely encountered in various industrial applications [1–5]. Due to strong interparticle forces (e.g., van der Waals force for fine particles, liquid bridge force for wet particles), the particles tend to form agglomerates in a fluidized bed, which can deteriorate the fluidization quality in particle mixing and reduce the effective particle-fluid interactions in heat and mass transfers. In the case of highly cohesive particles, severe issues such as channelling, slugging, and defluidization may arise in a fluidized bed [4,6]. Hence, it is important to understand the agglomeration of cohesive particles and propose the corresponding effective methods in assisting their fluidization.

In the past decades, as a cost-effective alternative to experimental techniques, various numerical methods have been developed to study fluidized bed systems [7–14]. Depending on the treatment of the solid/particle phase, there are two main types of numerical approaches. The first type is the continuum approach [14], like the Two-fluid model (TFM), in which the particle phase is treated as continuum media with the solid dynamics described using constitutive equations such as the kinetic theory of granular flow (KTGF); it is computationally efficient but difficult to describe the interparticle forces among cohesive particles explicitly. The second type is the discrete approach, like the coupled approach of combined computational fluid dynamics and discrete element method (CFD-DEM) [8,9,15], where the solid phase is treated as individual particles and the interparticle forces like van der Waals force, liquid bridging force, and electrostatic force are explicitly described. Because of the explicit consideration of interparticle forces, CFD-DEM has been increasingly used in studying the fluidization of cohesive particles [16–36].

Regardless of the type of particle cohesion (van der Waals or liquid bridge forces), previous studies obtained some general findings about the effects of particle cohesion. For instance, compared with the fluidization of non-cohesive particles, the fluidization of cohesive particles can experience, depending on the degree of particle cohesion, a significant agglomeration of particles, worse particle mixing, reduced circulation of particles, and defluidization of the bed [24–26,37–40]. To assist the fluidization of cohesive particles, relevant technologies include the use of a pulsed fluid flow, the addition of coarse particles, and vibrating and spouted beds. Among them, the spouted bed or spouted fluidized bed is relatively easy to design and implement. Some researchers have conducted studies on the fluidization of cohesive particles in spouted beds or spouted fluidized beds [26,30,33,41,42]. For example, He and her coworkers [26,42] studied the fluidization behaviors of wet particles in spouted fluidized beds and found that multiple-spouted fluidized beds can facilitate particle mixing and provide more space for particle mass and heat transfer. Xu et al. [30] analyzed the variable magnitudes of cohesive forces on fluidization behaviors in a spouted bed and found that defluidization occurs when the magnitude of the cohesive force reaches about 20 times of particle weight. Recently, Luo et al. [33] analyzed the deflection behaviors of wet particles in a spouted fluidized bed and found that the spouted deflection amplitude of wet particles is smaller than that in the bed of dry particles. Previous studies were mainly focused on the effects of particle cohesion on general fluidization behaviors like particle distribution, particle velocity distribution, and the circulation of solids in the bed. The fundamental issue regarding how the spouted bed or spouted fluidized bed can contribute to particle agglomeration or deagglomeration (compared with conventional fluidized beds) has not been well addressed yet. The understanding of such fundamental issue may

promote the optimal design and operation of the bed [42–48], thus potentially mitigating the practical problems like the observed defluidization of particles at strong cohesiveness of particles [30].

This study aims to understand the agglomeration and defluidization of cohesive particles (due to van der Waals force) in a fluidized bed, with a focus on how to assist the fluidization of cohesive particles using spouted gas flow. The methodology will be based on the numerical approach by CFD-DEM (due to its explicit consideration of interparticle force), which will be described in Section 2. In Section 3, the results and discussion will start with testing the significant effects of varying particle cohesion on the mixing and agglomeration behaviors; then, the limit of a conventional flat-bottom fluidized bed on the fluidization of very cohesive particles will be identified, through the analysis of typical agglomerates; to overcome the deficiency of a conventional fluidized bed, different designs of spouted beds and spout fluidized beds will be compared and analyzed towards assisting the fluidization of cohesive particles. Finally, Section 4 will summarize the key findings of this study.

2. Simulation method and conditions

2.1. Model description

The CFD-DEM model in this work is developed based on the open-source program CFDEM coupling [49,50], which combines the DEM package LIGGGHTS [51] and the CFD package OpenFOAM [52].

The dynamics of the solid phase are described by the particle scale DEM, which can trace and compute the forces and positions of individual particles explicitly. In DEM, the translational and rotational motions of individual particles are governed by the force and torque balances, which are written as:

$$m_i \frac{d\mathbf{v}_i}{dt} = \sum_j \left(\mathbf{F}_{n,ij} + \mathbf{F}_{t,ij} + \mathbf{F}_{coh,ij} \right) + \mathbf{F}_{pf,i} + m_i \mathbf{g} \tag{1}$$

and

$$I_i \frac{d\boldsymbol{\omega}_i}{dt} = \sum_j \left(\mathbf{T}_{t,ij} + \mathbf{T}_{r,ij} \right) \tag{2}$$

where m_i, $\mathbf{v}_i$, $\boldsymbol{\omega}_i$ and I_i are the mass, translational velocity, rotational velocity, and the moment of inertia of the particle i. The forces between particles include the normal contact force $\mathbf{F}_{n,ij}$, tangential contact force $\mathbf{F}_{t,ij}$, and cohesive force $\mathbf{F}_{coh,ij}$. The contact forces are calculated based on the Hertz model which considers the normal force $\mathbf{F}_{n,ij}$ and tangential force $\mathbf{F}_{t,ij}$, each of which incorporates both an elastic force term and a damping force term. The cohesive force $\mathbf{F}_{coh,ij}$ in this study is the van der Waals force with the same form as used in previous studies [15,53], expressed as $\mathbf{F}_{coh,ij} = -\frac{H_a}{6} \times \frac{64 R_i^3 R_j^3 \left(h + R_i + R_j \right)}{\left(h^2 + 2 R_i h + 2 R_j h \right)^2 \left(h^2 + 2 R_i h + 2 R_j h + 4 R_i R_j \right)^2} \overrightarrow{\mathbf{n}}_{ij}$, where Ha is the Hamaker constant, and h is the separation of surfaces along the line of the centers of particles i and j with a minimum separation h_{min} assumed as $1e^{-9}$ m for representing the repulsive nature between interacting particles. $\mathbf{F}_{coh,ij}$ is introduced by adding a header file of the cohesion force model (i.e., *cohesion_model_vdw.h*) in LIGGGHTS. Meanwhile, there are also other types of cohesion force formulations for fine particles (e.g., [20,24,54,55]), which can also be implemented in DEM/CFD-DEM models. The particle-fluid interaction force $\mathbf{F}_{pf,i}$ consists of three types of forces: drag, pressure gradient and viscous forces, with similar formulations as described in the reference [56]. Specifically, the used drag formulation is the one proposed by Koch and Hill [57], because it was used by the same open-source in its validation against

experimental data [50]. Nevertheless, it is noted that there are multiple drag formulations available, some of which may be more applicable in certain conditions, as discussed by Marchelli et al. [58]. The torques acting on particle i due to particle j include two components: $\mathbf{T}_{t,ij}$ which is generated by the tangential force and $\mathbf{T}_{r,ij}$ which is known as the rolling friction torque that is calculated by the constant directional torque (CDT) model in this study.

The fluid flow is described by CFD, with the governing equations of mass and momentum balances expressed as:

$$\frac{\partial\left(\rho_f\alpha_f\right)}{\partial t} + \nabla \bullet \left(\rho_f\alpha_f\mathbf{u}_f\right) = 0 \tag{3}$$

$$\frac{\partial\left(\rho_f\alpha_f\mathbf{u}_f\right)}{\partial t} + \nabla \bullet \left(\rho_f\alpha_f\mathbf{u}_f\mathbf{u}_f\right) = -\alpha_f\nabla p + \mathbf{F}_{fp} + \nabla \bullet \left(\alpha_f\tau_f\right) \tag{4}$$

where α_f, ρ_f, and $\mathbf{u}_f$ are the volume fraction occupied by the fluid, fluid density, and fluid velocity, respectively. τ_f is the stress tensor for the fluid phase. Because the current CFD-DEM model adopts the model A or set II as described by Zhou et al. [59], $\mathbf{F}_{fp}$ represents the particle based drag forces assembled in each computational cell. Since the used force and torque terms in this work are not new and have been clearly given in previous papers, they are not repeated here for clarity; interesting readers are suggested to see the previous paper [56] and the documentation [49,51] for detailed equations.

2.2. Simulation conditions

Two types of bed geometries are considered in this work. The first type is the conventional flat-bottom fluidized bed (to be used in Sections 3.1 and 3.2), which is a three-dimensional (3D) cuboid container, with a width of 60 d_p, thickness of 12 d_p, and bed height of 900 d_p. The second bed type consists of spouted beds with different designs of conical bed bottoms, which will be described in Section 3.2. Considering the used CFD sizes normally range from 2 to 4 d_p in previous studies (e.g., [19,26]), the size for CFD meshes in this work is about 3 $d_p \times 3 d_p \times 3 d_p$ in the cuboid/rectangular region, but the mesh sizes decrease significantly in the conical region in spouted beds. Therefore, a particle is possibly larger than a mesh in the conical region, which is treated by using the "bigParticleVoidFraction" model [49,50].

The simulation starts with a random generation of nonoverlapped spherical particles in the bed, followed by a settling process under gravity. Then, the packed bed is used as the starting point of fluidization. For the conventional flat-bottom fluidized bed, the inlet gas is uniformly injected from the bed bottom with the size of 60 $d_p \times 12 d_p$. The inlet gas flow conditions in spouted and spouted fluidized beds will be described in Section 3.2. Under all the considered flow conditions in this work, the particle Reynolds number (given by $Re_p = \frac{\alpha_f\rho_f d_p|\mathbf{u}_f - \mathbf{v}_p|}{\mu_f}$) is generally smaller than 50, corresponding to the laminar flow region; thus the simulation does not include a turbulence model.

Each simulation case computed the dynamics of 30,000 particles, for a duration about 1.5 s, with the DEM time step about 1.0×10^{-6} s and CFD time step about 5.0×10^{-6} s. Such computation may be much higher than that of the continuum approach like TFM. Nevertheless, thanks to the small simulation domain and the multiple cores (e.g., 4 or 8) used for the parallel computation, the computational time for each case is within 24 h and is thus acceptable for the fundamental research of this work.

Table 1 lists the key variables/parameters (in SI units) used in this study. It is noted that the particle diameter is kept constant at 100 μm in this work, while the particle cohesion strength is varied with the change of the Hamaker constant (*Ha*) with the range from 0 to 6.5×10^{-20} J. To achieve an easy quantitative understanding of cohesion strength, the *Ha* of particles is converted to a Bond number (*Bo*), defined as the ratio of the maximum cohesive force (at a specific *Ha* value) to the gravitational

Table 1
Parameters used in the current simulations.

Parameters	Values
Particle diameter, d_p	0.0001 m
Particle density, ρ_p	1200 kg m^{-3}
Young's modulus, E	1.0×10^7 Pa
Poisson ratio, δ	0.3
Coefficient of restitution, e	0.95
Coefficient of sliding friction, μ_s	0.3
Coefficient of rolling friction, μ_r	0.01
Hamaker constant, Ha	0–6.5×10^{-20} J
Fluid density, ρ_f	1.2 kg m^{-3}
Fluid viscosity, μ_f	1.5×10^{-5} kg m^{-1} s^{-1}
CFD cell size, $\Delta x \times \Delta y \times \Delta z$	$3\,d_p \times 3\,d_p \times 3\,d_p$
Bed width, $N_{cell,x}$	20
Bed thickness, $N_{cell,y}$	4
Bed thickness, $N_{cell,z}$	300

force. Even though the *Bo* number for group A powders may reach about 60 [38], the *Bo* numbers (e.g., 5, 10, 20, 30, 40) considered in this work do not correspond to specific materials and are mainly used for the fundamental understanding of particle cohesion effects on the fluidization behaviors.

It is noted that although the CFD-DEM model of this work is not directly validated by experiments, it is developed from an open source that has been validated through various experimental datasets and has been demonstrated to be well applicable in the past decade [36,49,50]. Meanwhile, under similar simulation conditions, we checked the minimum fluidization velocity (U_{mf}) simulated by the current model (U_{mf} about 0.007 m/s), being similar to that in previous studies [19,60]. Therefore, we believe the obtained results by the current model at least could be used for qualitative understanding of the fundamental issues, e. g., the general trend/mechanism regarding particle agglomeration/ deagglomeration under various (spout-assisted) fluidization conditions.

3. Results and discussion

3.1. Fluidization in a conventional flat-bottom bed

3.1.1. Particle mixing

The general fluidization patterns are firstly characterized by particle mixing, which is a basic function of fluidized beds in industrial applications [61,62]. In this work, a particle-scale mixing index (PSMI) [63–65] is used to quantify the mixing behaviors. As an extension of Lacey's index, PSMI further considers the results of the immediate neighborhood of each particle that can be well connected with the DEM outputs (e.g., particle contacts or coordination number). Similar to the calculation of various mixing indexes, the calculations with PSMI also need to determine a sample size that is set as the instantaneous average particle contact number (or coordination number). In the counting of contact numbers, two particles are considered to be in contact if their interparticle gap is smaller than a critical distance σ_{gap}. For dense particle flows where most particles have multiple contacts with their neighbours, σ_{gap} was set to a small value, such as 0.05 d_p in some previous studies [63–65]. By comparison, many particles in a fluidized bed may be located in a very dilute region, where a particle may even have no contact with its neighbours [60]. Therefore, σ_{gap} is set as 1.0 d_p in this study to ensure that most particles will have neighbours for calculating their mixing states. It is noted that the specific setting of σ_{gap} has a direct effect on the sample size of neighboring particles being counted, but may not result in a noticeable difference in PSMI at the final stage, because a weighting factor is used in the calculation of PSMI to account for the effect of sample size not being constant in the system [63–65].

The mixing behaviors of different cohesive particles (indicated by *Bo*) at $u_f = 0.15$ *m/s* are shown in Fig. 1. At a low cohesion strength, e.g., $Bo \leq 10$, the effect of cohesion on the mixing behaviors is not very obvious. The mixing of particles at $Bo = 10$ is quite similar to that at Bo
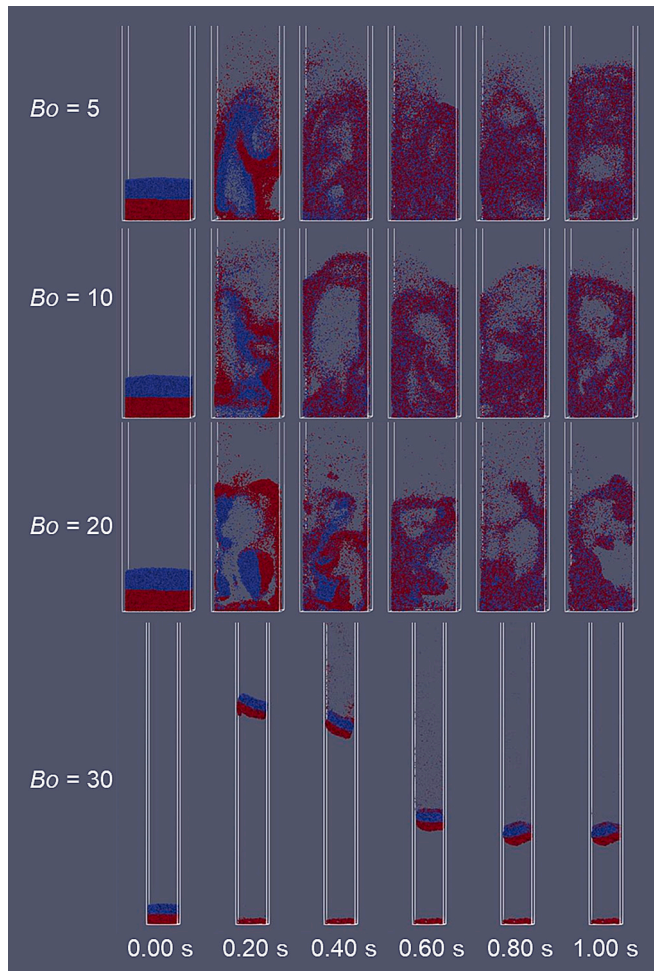
Fig. 1. Mixing of cohesive particles ($Bo = 5$–30) in the fluidized beds at gas inlet velocity $u_f = 0.15$ m/s; note that different bed heights are visualized due to different regions of interest, but their actual bed dimensions are the same for all the cases.

$= 5$. It is observed that dynamic bubbles quickly promote the mixing of particles (see the supplementary video S1 for more information); both achieve good mixing of particles around $t = 0.4$ s (see Fig. 2). By
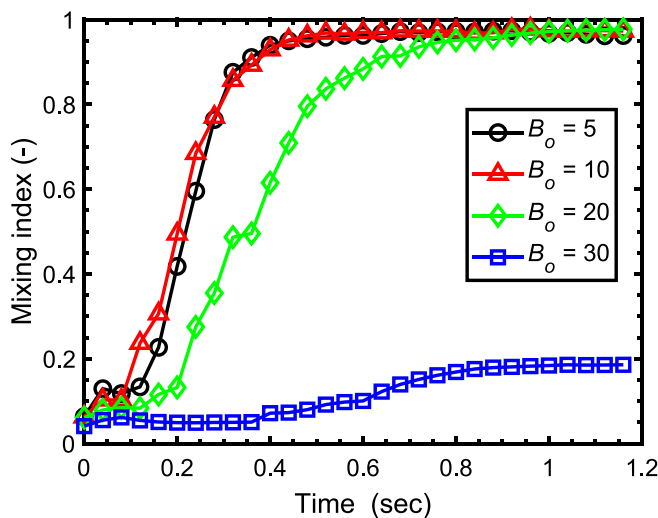

Fig. 2. Evolution of particle mixing index of cohesive particles ($Bo = 5$–30) at gas inlet velocity $u_f = 0.15$ m/s.

comparison, when the cohesion strength increases to a higher value, e. g., $Bo = 20$, fluidization behaviors become much different with less dynamic bubbles travelling through the bed (see the supplementary video S1 for more information). Accordingly, the mixing of particles at $Bo = 20$ becomes much worse and takes longer (about $t = 0.8$ s) to reach a good mixing state, as shown in Fig. 2. With the further increase of particle cohesion to $Bo = 30$, the bed is not fluidizable anymore. Instead of being dispersed by gas bubbles passing through, a large block of particles consistently remains as an agglomerate, significantly impeding particle mixing.

3.1.2. Particle agglomeration

Section 3.1.1 has shown that the deterioration of particle mixing at higher cohesion strength is related to the agglomeration of particles. Here, the particle agglomeration will be further characterized. This work employs an algorithm similar to the one proposed in a previous study [31], which identifies particle agglomerates through a recursive search of particle contacts. It is noted that the previous study [31] focused on fundamental correlations regarding solid pressure of granular flow, using a strict yet computationally expensive way to obtain the enduring contacts of particles over a certain period of time (e.g., 100 DEM time steps). By comparison, this study, which focuses more on general flow patterns, interprets data qualitatively and thus utilizes instantaneous particle contacts for identifying agglomerates. This approach efficiently captures the effects of particle agglomeration on flow patterns, while being more computationally efficient than the search for enduring contacts.

The agglomerates in the fluidized beds of different cohesive particles are characterized in Fig. 3, with their size distribution shown in Fig. 4. Here, the size of an agglomerate is defined as the number of original
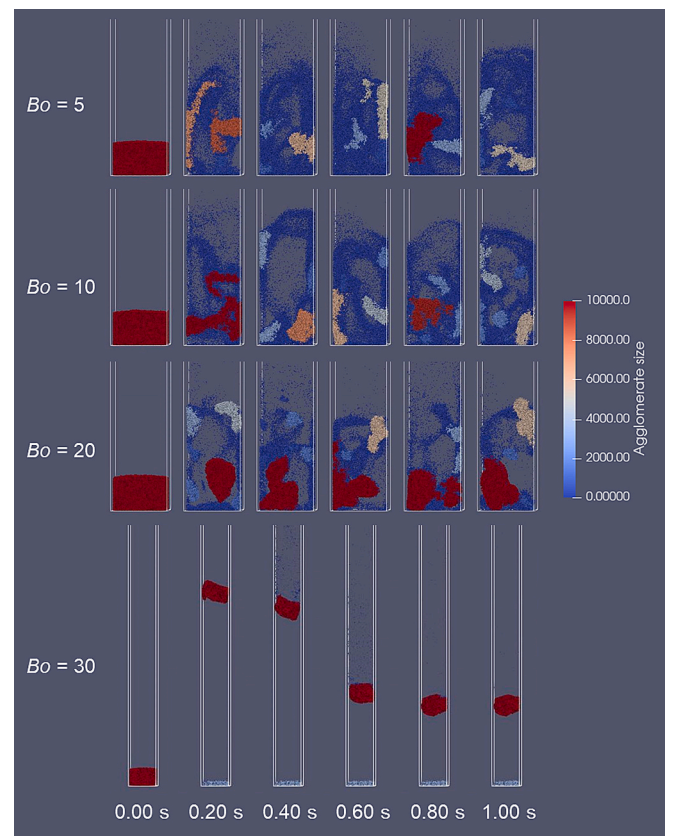

Fig. 3. Agglomeration of cohesive particles ($Bo = 5$–30) in the fluidized beds at $u_f = 0.15$ m/s; note that different bed heights are visualized due to different regions of interest, but their actual bed dimensions are the same for all the cases.
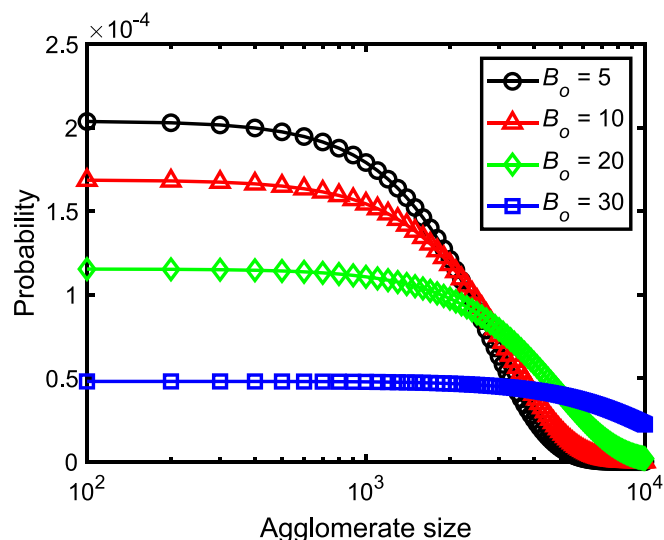
Fig. 4. Distribution of agglomerate size (by the number of original particles) of cohesive particles ($Bo = 5$–30) at gas inlet velocity $u_f = 0.15$ m/s.

Fig. 5. Agglomeration of highly cohesive particles at $Bo = 30$ (top row) and $Bo = 40$ (bottom row) in the fluidized beds at $u_f = 0.5$ m/s.

particles within this agglomerate body, represented by different colours. At a lower cohesion strength (e.g., $Bo \leq 10$), the formation and breakage of agglomerates in the bed are very dynamic; some large-sized agglomerates (red ones in Fig. 3) are formed at certain time instants, but are quickly deagglomerated at the next time instant. Meanwhile, there is still a large fraction of individual or very small-sized agglomerates (indicated by those blue ones in Fig. 3 and the distribution curves in Fig. 4), being dispersed in the bed. This accounts for the good mixing of particles shown in Fig. 1. At a higher cohesion ($Bo = 20$), large-sized agglomerates are consistently formed, taking up a significant space in the bed, especially at the bed bottom. A large group of particles in those agglomerates are consistently in contact with their neighbours and cannot move freely, thus the mixing of particles is more difficult. With the further increase of particle cohesion ($Bo = 30$), most particles are strongly connected with their neighbours and cannot be detached by the fluid flow anymore, resulting in the failure of fluidization.

Previously, it was shown that a higher gas velocity may enhance the particle-fluid interactions that can break the large agglomerates and facilitate fluidization [31]. Then, a high velocity of $u_f = 0.5$ m/s (about 70 u_{mf}) is used as the inlet gas velocity, with the results shown in Fig. 5. As expected, the higher gas velocity promotes the breakage of large agglomerates, facilitating the fluidization of cohesive particles. Notably, at this increased velocity, the bed of particles at $Bo = 30$, previously non-fluidizable at a lower velocity ($u_f = 0.15$ m/s), achieves fluidization at $u_f = 0.5$ m/s.

However, it is noticed that the fluidization remains difficult at a higher Bo, e.g., $Bo = 40$. While initial fluidization is achieved, a large agglomerate eventually forms at the bed bottom, leading to fluidization failure over time (e.g., $t > 1.0$ s). This indicates that the formation of large agglomerates can actually lead to the defluidization of the bed. Additionally, it is observed that some particles have already reached the top of the bed, indicating the bed at $u_f = 0.5$ m/s has nearly reached the pneumatic conveying state and a further increase of gas velocity may not be effective. It would be interesting to understand how can we readily achieve the fluidization of such highly cohesive particles. This will be discussed in the following sections.

3.1.3. Analysis of typical agglomerates

As shown in the previous sections, significant agglomeration of particles can hinder particle mixing and potentially cause the defluidization of a bed. Then, it is of fundamental importance to understand the dynamics of lar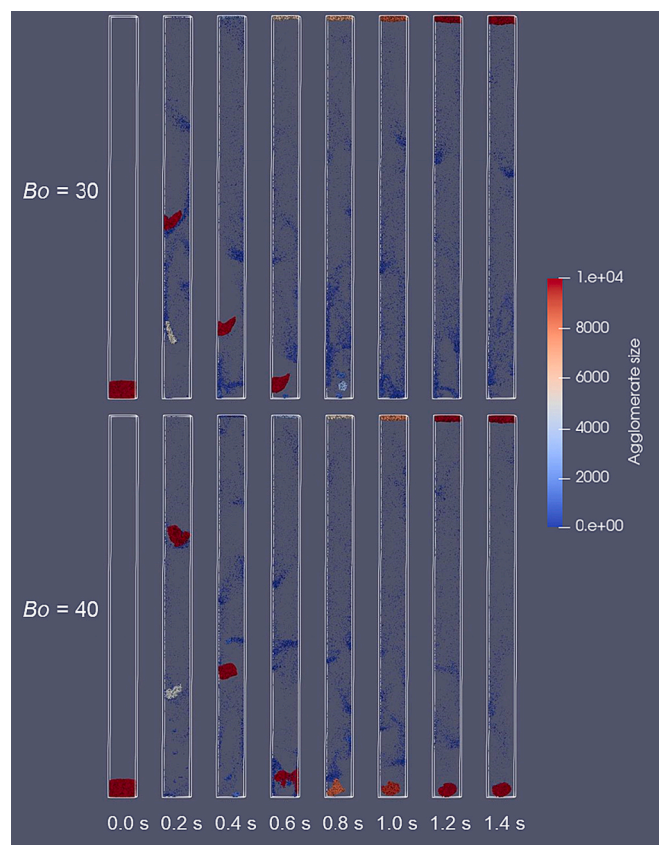ge-sized agglomerates in a fluidized bed. Accordingly, the dynamic evolution of typical agglomerates at $Bo = 40$ (as identified in Fig. 5) is traced and analyzed in this section.

Fig. 6 displays the dynamic evolution of the deagglomeration of a typical large-size agglomerate (more dynamics can be seen in supplementary video S2). At the beginning ($t = 0.852$ s), the fluid flow velocity has reached around 2 m/s (which is much higher than the inlet gas velocity of 0.5 m/s) in the confined channel between the agglomerate and the bed wall at the left side, as depicted in Fig. 6 (a-1) and Fig. 6 (b-1). This causes a heterogeneous distribution of both drag forces and particle velocities within the agglomerate. Especially, the left and right sides of the agglomerate have opposite horizontal orientations (x direction) in terms of drag forces (Fig. 6 (a-2)) and particle velocities (Fig. 6 (b-2)). Such differences in particle properties facilitate the development of a crack within the porous part (i.e., lower solid fraction) of the agglomerate (see Fig. 6 (c-2) and Fig. 6 (c-3)). The crack at the lower solid fraction region corresponds to both a weaker mechanical strength part of the agglomerate and a lower frictional resistance part to the gas flow. As a result, strong gas preferentially flows through the crack region, causing the further development of the crack and the corresponding breakage of the agglomerate (see snapshots at $t = 0.868$ s and $t = 0.872$ s).

Fig. 7 shows a stabilized agglomerate in the fluidized bed. Instead of going through the middle part of the agglomerate (as shown in Fig. 6), the gas flows primarily bypass the agglomerate, going through the left and right sides near the bed walls. Therefore, despite high fluid velocities (e.g., near 2 m/s), the fluid flows do not result in effective particle-fluid interactions. As a result, unlike the observations in Fig. 6, there is no evident development of a porous weak part in this stabilized agglomerate, thus the breakage or deagglomeration of the structure does not happen. As such, to realize the deagglomeration or breakage of large agglomerates for the fluidization of cohesive particles, it is critical to
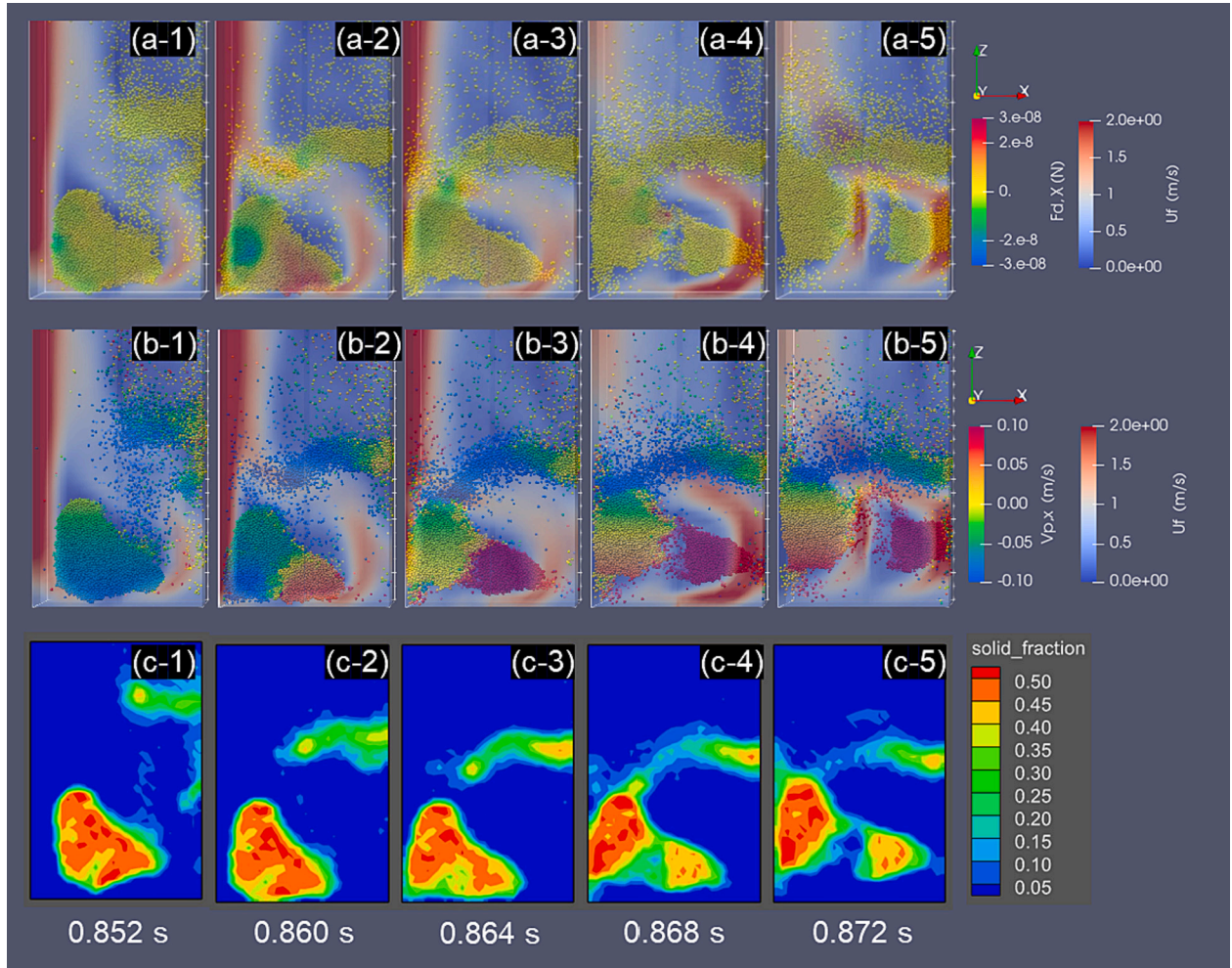
Fig. 6. Evolution of a typical agglomerate identified at $Bo = 40$ and $u_f = 0.5$ m/s, where the top, middle, and bottom rows correspond to drag force at x direction ($\mathbf{F}_{d, x}$), particle velocity at x direction ($\mathbf{V}_{p, x}$), and solid fraction. Note that the x direction is oriented towards the right of the horizontal axis, as indicated in the orientation axes.

ensure effective particle-fluid interactions, with avoiding the bypassing of the fluid flows around the agglomerates. Given this, spouted or spouted fluidized beds, known for creating strong particle-fluid interactions, appear promising for the efficient fluidization of cohesive particles.

3.2. Spout-assisted fluidization of highly cohesive particles

3.2.1. Bed geometry and spouted flow conditions

In this section, both spouted bed (with only central spouted gas flow) and spouted fluidized bed (with both central spouted and background gas flows) will be utilized for aiding the fluidization of highly cohesive particles with $Bo = 40$, which cannot be well fluidized by the conventional fluidized bed (see Sections 3.1 and 3.2). As the conical geometry of the bed bottom can have important influences on fluidization behaviors [47,66], three types of conical bottom designs are considered. As shown in Fig. 8, the three beds have different angles of slope θ at the bottom next to the central orifice. Except for the angle θ, the central orifice size for the spouted gas flow is kept the same ($6 d_p$). Apart from the difference in bottom geometry, the width ($60 d_p$), thickness ($12 d_p$), and height ($900 d_p$) of the bed are kept the same as the flat-bottom bed studied in Sections 3.1 and 3.2.

The spouted gas velocities (U_{sg}) and background gas velocities (U_{bg}) in the bed of each case are shown in Table 2. It is noted that although the considered cases have some differences (e.g, in the bed types, θ, and/or

the gas velocities), the total flow rate of inlet gas from the bottom of the bed is kept at a similar value as the case of $U_f = 0.5$ m/s for the conventional flat-bottom bed in Section 3.1 or Section 3.2 (such as the case displayed in Fig. 5). By keeping the total gas flow rate similar, the effects of spouted gas flow conditions (i.e., spouted or spouted fluidized condition) and the bed bottom geometries (i.e., θ) can be more clearly identified.

3.2.2. Flow patterns

The flow patterns of the cases described in Table 2 are shown in Fig. 9. In general, due to the spout flow, a strong jet of gas is created in the bed, which helps the deagglomeration or breakage of the agglomerates in the start-up phase (e.g., as the snapshot at 0.04 s). After the start-up, agglomerates are more frequently observed at the bottom of the bed. With the V-shaped bottom of the bed, particles or agglomerates are guided towards the centre of the bottom, where the strong spouted flow leads to strong particle-fluid interactions. The effectiveness of the particle-fluid interactions on the deagglomeration is related to the condition of the spouted gas flow and the angles of slope (i.e., θ). It is observed that the spouted fluidized beds may be less effective than spouted beds in the deagglomeration of particles, under the conditions considered in this work (Table 2). For example, in Case-4 and Case-6, the large-size agglomerates are not effectively broken up by the gas flow and remain in the bottom of the beds (e.g., from 1.26 s to 1.48 s). By comparison, spouted beds with high spouted velocities appear to be more
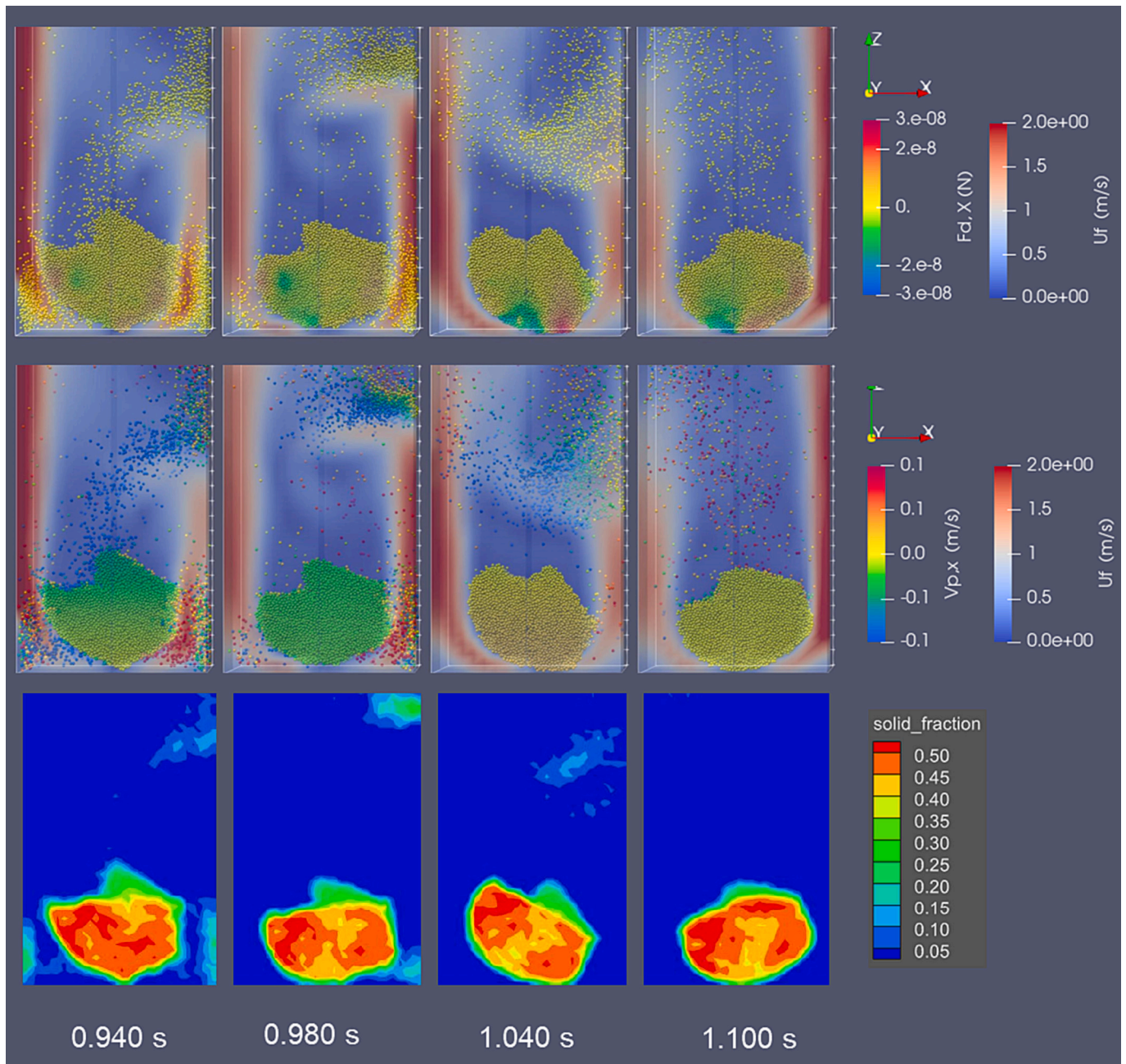
Fig. 7. A stable agglomerate (identified at $Bo = 40$ and $u_f = 0.5$ m/s) in the fluidized bed, where the top, middle, and bottom rows correspond to drag force at x direction ($\mathbf{F}_{d, x}$), particle velocity at x direction ($\mathbf{V}_{p, x}$), and solid fraction.

effective in the deagglomeration of agglomerates, especially at a larger θ. For instance, in Case-3 ($\theta = 60°$), when a large-size agglomerate formed in the bottom (e.g., 1.09 s), the strong spouted flow in the confined space creates strong drag forces on particles; subsequently, instead of bypassing the agglomerate (as observed in snapshots from 1.26 s to 1.48 s in Case-4 and Case-6), the central spouted flow directly breaks up the agglomerate in the central part (see snapshot at 1.26 s in Case-3) and results in the effective deagglomeration.

3.2.3. Agglomeration and mixing

To gain a more quantitative comparison, the distribution of agglomerate size and the evolution of the mixing index are shown in Fig. 10. For spouted beds (Cases 1–3), an increase of θ results in a higher probability of smaller agglomerate sizes (and lower probability in larger agglomerate sizes), as well as a noticeable improvement in the mixing

index. This indicates that it might be helpful to increase θ of the spouted bed to improve deagglomeration effectiveness and fluidization quality. The underlying reason might be that a larger θ corresponds to a more confined space near the spouted flow, thus enhancing the particle-fluid and particle-wall interactions for more effective deagglomeration and corresponding better mixing of particles. This will be further analyzed in Section 3.2.4.

Because of the introduction of background gas flow and the reduced velocity in the spouted gas flow in the spouted fluidized beds (see Table 2), the relationship between fluidization quality and θ in Cases 4–6 is quite different from that in Cases 1–3 (spouted beds). For example, it is $\theta = 45°$ that corresponds to the higher probability of smaller agglomerate size, while $\theta = 30°$ corresponds to the best mixing of particles. By comparison, $\theta = 60°$, which results in the best fluidization quality in the spouted bed (i.e., Case-3), corresponds to the nearly lowest probability
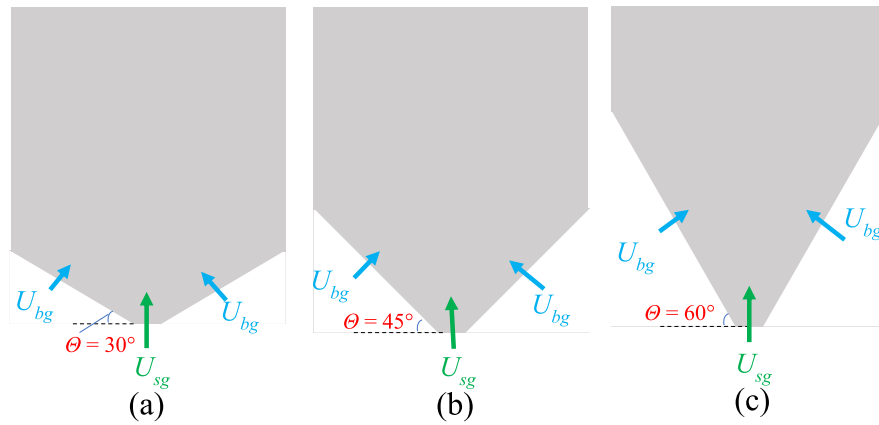
Fig. 8. Geometry of three different bottom designs of the spouted or spouted fluidized beds.

Table 2
Parameters for the geometry and gas flows of the beds.

Case no.	Bed type	Θ (deg.)	U_{sg} (m/s)	U_{bg} (m/s)	Inlet volumetric gas flow rate (m³/s)
1	Spouted bed	30	5.0	0	3.60×10^{-10}
2	Spouted bed	45	5.0	0	3.60×10^{-10}
3	Spouted bed	60	5.0	0	3.60×10^{-10}
4	Spouted fluidized bed	30	3.0	0.195	3.62×10^{-10}
5	Spouted fluidized bed	45	3.0	0.156	3.59×10^{-10}
6	Spouted fluidized bed	60	3.0	0.111	3.60×10^{-10}

in smaller agglomerate size and the worst mixing of particles in the spouted fluidized bed (Case-6). This illustrates that instead of being merely influenced by bed geometry, their fluidization behaviors should result from the interplay of multiple effects, which will be further discussed in the following section.

3.2.4. Mechanisms underlying spout-assisted fluidization

This section will further explore the mechanisms underlying the functions and effectiveness of spout-assisted deagglomeration and fluidization of highly cohesive particles. Particle dynamics in various spouted and spout-fluidized beds will also be compared, for understanding the fluidization performance observed in previous sections.

Based on the observations from Sections 3.2.2 and 3.2.3, it is known that the spouted bed with $\theta = 60°$ achieved the highest fluidization quality. To examine the underlying reasons, Fig. 11 displays a typical deagglomeration process of a large agglomerate (relevant information is also shown in supplementary video S3). It is noted that this agglomerate is identified for the time beyond $t = 1.0$ s, when the developed significant agglomeration may not be able to be deagglomerated in a conventional flat-bottom bed (see Figs. 5 and 7). As shown in Fig. 11, at $t = 1.000$ s, this large agglomerate is located near the central spouted orifice (under the function of inclined side walls). Accordingly, this large and dense agglomerate confines the space for the central spouted flow to mainly go through the channel between the agglomerate and the side walls (snapshots at $t = 1.000$ s, 1.188 s, and 1.236 s), which results in significant drag forces on particles. The enhanced drag forces drive the agglomerate to vigorously hit the side walls, which creates significant particle-wall interaction forces impacting the agglomerate (which can be clearly observed in the supplementary video S4). As a result, the agglomerate structure is gradually loosened, as shown by the distribution of solid fraction. Especially, porous weak parts with low solid fraction (indicated by the black dash circles) appear and increasingly grow in the agglomerate, resulting in the final deagglomeration of the structure.

Hence, similar to the observation and analysis in Section 3.1.3, the appearance/creation of those porous weak parts, which are both low in mechanical strength and preferred by the fluid flow, may be critical for realizing a successful deagglomeration process. Such weak parts are difficult to develop in a conventional bed with a flat and more spacious bottom structure (Fig. 7), but are readily created under the enhanced particle-fluid and particle-wall interactions in the confined spouted bed with a conical structure.

From such observations, it is known that the effectiveness of the spouted bed in assisting the deagglomeration may be attributed to its function in promoting the gathering of particles/agglomerates in the central orifice part, where the particle-fluid and particle-wall interactions are enhanced to loosen the agglomerate structure until its final deagglomeration. Since the spouted bed with $\theta = 60°$ corresponds to a more inclined slope in promoting the flow of particles/agglomerates towards the orifice and possesses a more confined space for more significant particle-fluid and particle-wall interactions, it is more effective in facilitating a better deagglomeration/fluidization quality among others with smaller θ (as observed in Sections 3.2.2 and 3.2.3).

To further understand the functions and differences of various spouted and spout fluidized beds in aiding the fluidization of cohesive particles, the evolution of relevant key variables (including the drag force, particle velocity, and particle-wall contact force) as a function of time is compared, as shown in Fig. 12. Because it is known that the agglomeration-induced defluidization may occur after a certain period (Figs. 5 and 9), the tracing and comparison are conducted for the time beyond $t = 1.0$ s. Since significant agglomeration or defluidization is mainly developed in the bottom region of the bed (see Figs. 5, 7, 9, and 11), particle dynamics only in the bottom region with a height of 60 d_p are counted for the results here.

In general, the considered drag force, particle velocity, and particle-wall contact force are all significant in the spouted bed with $\theta = 60°$. This further explains its effectiveness in promoting the deagglomeration and fluidization quality. By comparison, both forces and particle velocity in the spout fluidized bed with $\theta = 60°$ are very weak. The reason might be that $\theta = 60°$ corresponds to a faster gathering of particles/agglomerates in a smaller space confined by the side walls. Those large agglomerates can be effectively broken up by the high spouted gas velocity in a spouted bed, but may not be effectively broken up by the lower spouted gas velocity in a spout fluidized bed (as observed from the snapshots in Case-6 in Fig. 9).

For the spouted beds, the effects of θ variation on the considered forces and particle velocities are evident. The spouted bed with $\theta = 30°$, in which the drag force and particle velocity can also be significant, experiences very weak particle-wall interaction forces. This may be attributed to its flatter and less confined bottom structure. Because it is
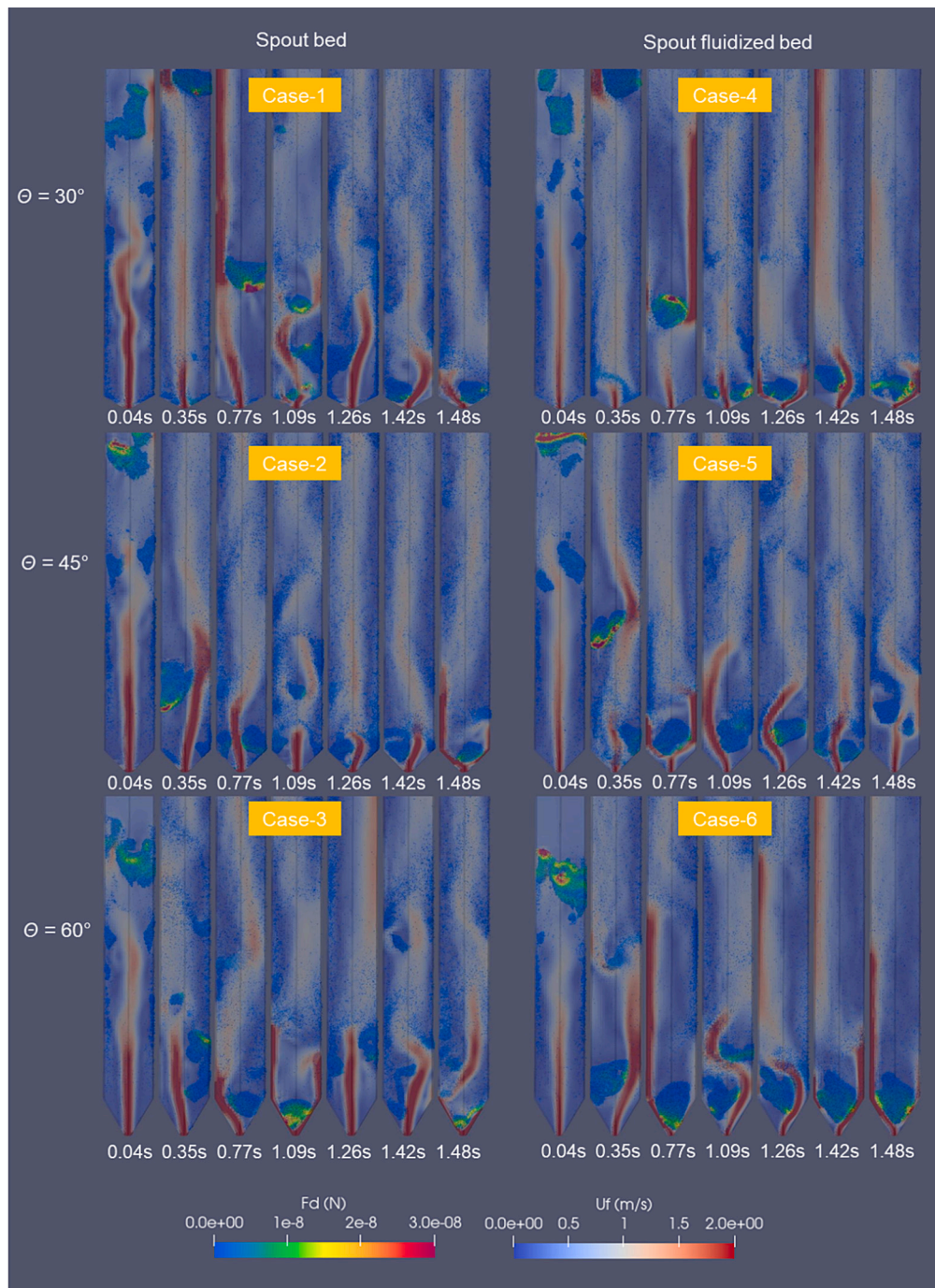
Fig. 9. Flow patterns at different instants of time of spouted beds (left side) and spouted fluidized beds (right side) described in Table 2, where the colours of particles indicate the magnitude of drag forces and the colours of fluid phase indicate the magnitude of fluid velocity.

shown that the magnitude of particle-wall force in the process can be much higher than that of drag force, the fewer particle-wall interactions in the spouted bed with $\theta = 30°$ may account for its less efficiency in aiding the deagglomeration and fluidization of the considered highly cohesive particles that cannot be easily deagglomerated by small forces. In contrast, the spouted bed with $\theta = 45°$ experiences significant particle-wall forces, but less pronounced drag force and particle velocity, compared with those in the spouted bed with $\theta = 60°$. Hence, it should be the combined contribution of both particle-wall and particle-fluid forces that facilitate the highest fluidization quality.

For the spout fluidized beds, the effects of θ variation on the considered forces and particle velocities are less evident. Nevertheless, it

can be seen that the spout fluidized bed with $\theta = 60°$ corresponds to the weakest forces and particle velocity, compared with others. This may account for its inefficiency in aiding fluidization, as observed in Sections 3.2.2 and 3.2.3. In addition, the performance of the spout fluidized beds may also be related to the spreading and directions of their background gases. As shown in Section 3.2.1, although the considered beds have similar inlet gas fluxes (Table 2), the increase of θ in spout fluidized beds witnesses the decrease of the background gas velocities and a more horizontal gas flow direction (Fig. 8). Accordingly, the spout fluidized bed with $\theta = 60°$ has the most spreading and the most horizontal background gas flows, which may account for its inefficiency compared with other spout fluidized beds. In contrast, the spout fluidized bed with
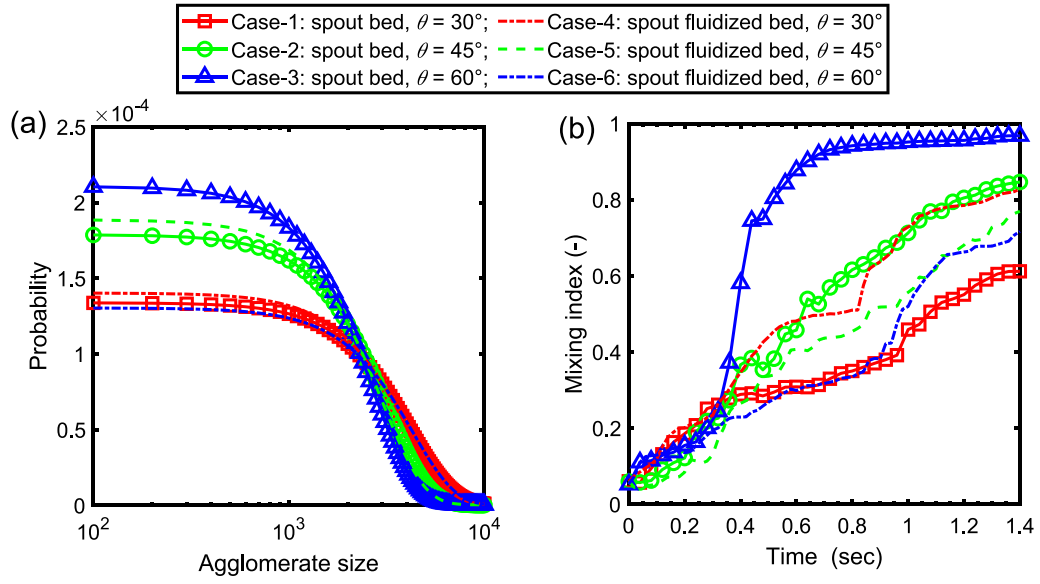
Fig. 10. Distribution of agglomerate size by the number of original particles (a) and the evolution of particle mixing index (b) in different spouted and spouted fluidized beds.
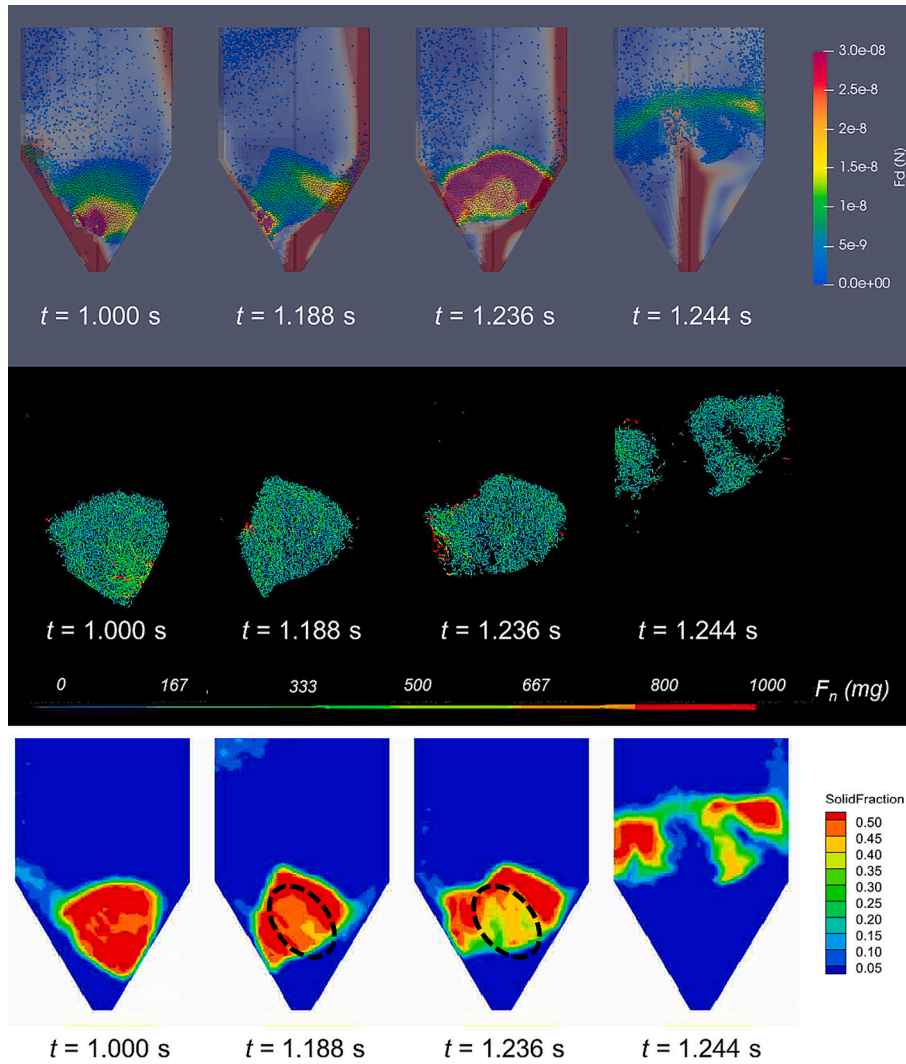

Fig. 11. Evolution of drag force (top row), normal contact force chain (middle row), and solid fraction (bottom row) in a typical deagglomeration process from the spouted bed with $\theta = 60°$.
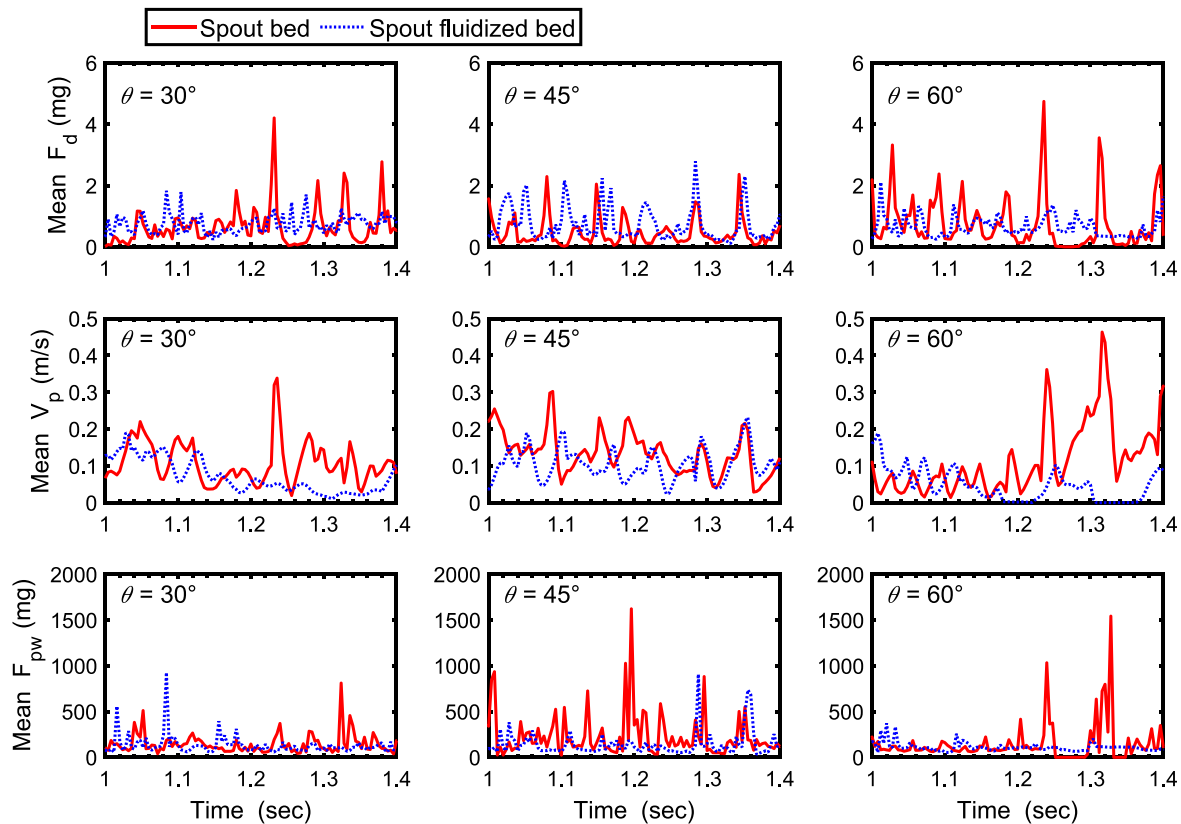
Fig. 12. Evolution of mean drag force (top row), mean particle velocity (middle row), and mean particle-wall contact force (bottom row) with time.

$\theta = 30°$ has the more concentrated background gas flows with a more vertical flowing direction, which may account for its best performance in promoting the mixing of particles, as observed in Section 3.2.3.

4. Conclusion

Based on numerical simulation by CFD-DEM, this work investigated the effects of particle cohesion (due to van der Waals force) on the agglomeration and defluidization of particles in fluidized beds, and explored the utilization of spouted gas flow for facilitating deagglomeration and fluidization quality. The main findings are summarized below:

(1) The effect of particle cohesion on fluidization behaviors becomes increasingly significant with the increase of cohesion strength indicated by Bo. At $Bo = 20$, large-sized agglomerates form in the bed and deteriorate the mixing quality of particles. At $Bo = 30$, fluidization is only achievable at a very high inlet gas velocity (e. g., $u_f = 0.5$ m/s, near the pneumatic conveying velocity in this study) in a flat-bottom fluidized bed. At $Bo = 40$, the large-sized agglomerates cannot be effectively broken up and this results in the defluidization of the bed.

(2) Large-sized agglomerates are most commonly formed in the bottom region of the bed, and their deagglomeration may start from a porous part (i.e., low solid fraction part within the agglomerate body), which is low in mechanical strength and preferred by the fluid flow. When particle cohesion is high (e.g., $Bo = 40$), such a weak part and corresponding deagglomeration are difficult to develop in a conventional flat-bottom bed, where the bypassing of fluid flows around the agglomerate may happen and result in defluidization.

(3) The spouted bed with inclined side walls in its conical bottom can promote the flow of particles and agglomerates towards the central spout orifice, with enhancing particle-fluid and particle-wall interactions for continuously loosening the agglomerate structure until realizing the final deagglomeration. With such functions, spouted beds can assist the deagglomeration and fluidization of highly cohesive particles (e.g., $Bo = 40$) that cannot be well fluidized in a conventional flat-bottom bed.

(4) The inclined angle θ of the side walls in the conical bed bottom is found to be critical in affecting the deagglomeration and fluidization behaviors. By keeping a similar inlet flow flux for a series of spouted and spouted fluidized beds with different conical geometries, the spouted bed with a large inclined angle of side walls ($\theta = 60°$) achieves the best fluidization quality in the deagglomeration and mixing of highly cohesive particles; the spout fluidized bed with a large θ (e.g., $60°$) is found less effective in facilitating deagglomeration and fluidization, due to its less concentrated and more horizontal background gas flows.

The obtained findings of this study offer fundamental insights for understanding the effective design and mechanisms of spout-assisted fluidization of cohesive particles, which may be relevant in various industrial applications. Nevertheless, it is noted that although the CFD-DEM model of this work is developed from an open source that has been widely used and demonstrated to be well applicable, the obtained findings of this work, without a detailed experimental validation yet, should be interpreted qualitatively, particularly regarding the effect of specific Bo and θ values. In future, suitable experiments for the model validation will be of great interest for generating more reliable quantitative insights, thus aiding the more practical design and optimization of relevant applications.

Supplementary data to this article can be found online at https://doi. org/10.1016/j.powtec.2024.119512.

CRediT authorship contribution statement

Yi Zou: Writing – review & editing, Writing – original draft, Investigation, Formal analysis, Data curation. **Ruiping Zou:** Writing – review & editing, Validation, Resources, Project administration, Investigation, Formal analysis. **Yongli Wu:** Writing – review & editing, Writing – original draft, Visualization, Validation, Software, Methodology, Investigation, Funding acquisition, Formal analysis.

Declaration of competing interest

The authors declare that they have no known competing financial interests or personal relationships that could have appeared to influence the work reported in this paper.

Data availability

Data will be made available on request.

Acknowledgements

References

[1] D. Geldart, Types of gas fluidization, Powder Technol. 7 (1973) 285–292.
[2] Z. Luo, M. Fan, Y. Zhao, X. Tao, Q. Chen, Z. Chen, Density-dependent separation of dry fine coal in a vibrated fluidized bed, Powder Technol. 187 (2008) 119–123.
[3] P. Gayán, C. Dueso, A. Abad, J. Adanez, L.F. de Diego, F. García-Labiano, NiO/Al2O3 oxygen carriers for chemical-looping combustion prepared by impregnation and deposition-precipitation methods, Fuel 88 (2009) 1016–1023.
[4] J.M.V. Millán, Fluidization of Fine Powders: Cohesive Versus Dynamical Aggregation, Springer Science & Business Media, 2012.
[5] Y. Zhou, J. Xu, J. Zhu, Different bubble behaviors in gas-solid fluidized bed of Geldart group a and group C+ particles, Powder Technol. 384 (2021) 431–441.
[6] J. Chaouki, C. Chavarie, D. Klvana, G. Pajonk, Effect of interparticle forces on the hydrodynamic behaviour of fluidised aerogels, Powder Technol. 43 (1985) 117–125.
[7] T.B. Anderson, R. Jackson, Fluid Mechanical Description of Fluidized Beds. Equations of Motion, Industrial & Engineering Chemistry Fundamentals 6, 1967, pp. 527–539.
[8] Y. Tsuji, T. Kawaguchi, T. Tanaka, Discrete particle simulation of two-dimensional fluidized bed, Powder Technol. 77 (1993) 79–87.
[9] N.G. Deen, M. Van Sint Annaland, M.A. Van der Hoef, J.A.M. Kuipers, Review of discrete particle modeling of fluidized beds, Chem. Eng. Sci. 62 (2007) 28–44.
[10] H.P. Zhu, Z.Y. Zhou, R.Y. Yang, A.B. Yu, Discrete particle simulation of particulate systems: a review of major applications and findings, Chem. Eng. Sci. 63 (2008) 5728–5770.
[11] S. Sundaresan, A. Ozel, J. Kolehmainen, Toward constitutive models for momentum, species, and energy transport in gas-particle flows, Annu. Rev. Chem. Biomol. Eng. 9 (2018) 61–81.
[12] W. Ge, Q. Chang, C. Li, J. Wang, Multiscale structures in particle–fluid systems: characterization, modeling, and simulation, Chem. Eng. Sci. 198 (2019) 198–223.
[13] B.W. Fitzgerald, A. Zarghami, V.V. Mahajan, S.K.P. Sanjeevi, I. Mema, V. Verma, Y.M.F. El Hasadi, J.T. Padding, Multiscale simulation of elongated particles in fluidised beds, Chem. Eng. Sci. X 2 (2019) 100019.
[14] J. Wang, Continuum theory for dense gas-solid flow: a state-of-the-art review, Chem. Eng. Sci. 215 (2020) 115428.
[15] H.P. Zhu, Z.Y. Zhou, R.Y. Yang, A.B. Yu, Discrete particle simulation of particulate systems: theoretical developments, Chem. Eng. Sci. 62 (2007) 3378–3396.
[16] T. Mikami, H. Kamiya, M. Horio, Numerical simulation of cohesive powder behavior in a fluidized bed, Chem. Eng. Sci. 53 (1998) 1927–1940.
[17] M.J. Rhodes, X.S. Wang, M. Nguyen, P. Stewart, K. Liffman, Onset of cohesive behaviour in gas fluidized beds: a numerical study using DEM simulation, Chem. Eng. Sci. 56 (2001) 4433–4438.
[18] M. Ye, M.A. Van Der Hoef, J.A.M. Kuipers, A numerical study of fluidization behavior of Geldart a particles using a discrete particle model, Powder Technol. 139 (2004) 129–139.
[19] Q.F. Hou, Z.Y. Zhou, A.B. Yu, Micromechanical modeling and analysis of different flow regimes in gas fluidization, Chem. Eng. Sci. 84 (2012) 449–468.
[20] T. Kobayashi, T. Tanaka, N. Shimada, T. Kawaguchi, DEM-CFD analysis of fluidization behavior of Geldart group a particles using a dynamic adhesion force model, Powder Technol. 248 (2013) 143–152.
[21] C. Pei, C.Y. Wu, D. England, S. Byard, H. Berchtold, M. Adams, Numerical analysis of contact electrification using DEM-CFD, Powder Technol. 248 (2013) 34–43.
[22] C. Thornton, F. Yang, J. Seville, A DEM investigation of transitional behaviour in gas-fluidised beds, Powder Technol. 270 (2015) 128–134.
[23] P. Liu, C.Q. LaMarche, K.M. Kellogg, C.M. Hrenya, Fine-particle defluidization: interaction between cohesion, Young's modulus and static bed height, Chem. Eng. Sci. 145 (2016) 266–278.
[24] D. Liu, B.G.M. van Wachem, R.F. Mudde, X. Chen, J.R. van Ommen, An adhesive CFD-DEM model for simulating nanoparticle agglomerate fluidization, AICHE J. 62 (2016) 2259–2270.
[25] Y. Gu, A. Ozel, S. Sundaresan, Numerical studies of the effects of fines on fluidization, AICHE J. 62 (2016) 2271–2281.
[26] Y. He, W. Peng, T. Tang, S. Yan, Y. Zhao, DEM numerical simulation of wet cohesive particles in a spout fluid bed, Adv. Powder Technol. 27 (2016) 93–104.
[27] J. Gan, Z. Zhou, A. Yu, CFD-DEM modeling of gas fluidization of fine ellipsoidal particles, AICHE J. 62 (2016) 62–77.
[28] R. Wilson, D. Dini, B. van Wachem, A numerical study exploring the effect of particle properties on the fluidization of adhesive particles, AICHE J. 62 (2016) 1467–1477.
[29] M. Wu, J.G. Khinast, S. Radl, The effect of liquid bridge model details on the dynamics of wet fluidized beds, AICHE J. 64 (2017) 437–456.
[30] H. Xu, W. Zhong, Z. Yuan, A.B. Yu, CFD-DEM study on cohesive particles in a spouted bed, Powder Technol. 314 (2017) 377–386.
[31] Y. Wu, Q. Hou, A. Yu, Linking discrete particle simulation to continuum properties of the gas fluidization of cohesive particles, AICHE J. 66 (2020) e16944.
[32] L. Hua, R. Ocone, N. Yang, CFD–DEM simulations of wet particles fluidization with a new evolution model for liquid bridge, AICHE J. 68 (2022) e17681.
[33] Z. Luo, Y. Yue, S. Wang, Y. Shen, CFD-DEM study of spout deflection behavior of cohesive particles in a spout fluidized bed, Powder Technol. 427 (2023).
[34] Y. Tsunazawa, D. Fujihashi, S. Fukui, M. Sakai, C. Tokoro, Contact force model including the liquid-bridge force for wet-particle simulation using the discrete element method, Adv. Powder Technol. 27 (2016) 652–660.
[35] Z. Ma, Q. Tu, Z. Liu, Y. Xu, R. Ge, H. Wang, CFD-DEM investigation of the gas-solid flow characteristics in a fluidized bed dryer, Chem. Eng. Res. Des. 196 (2023) 235–253.
[36] X. Liu, C.J.M. Hessels, N.G. Deen, Y. Tang, CFD-DEM investigation on the agglomeration behavior of micron-sized combusted iron fines, Fuel 346 (2023).
[37] C. Song, D. Liu, J. Ma, X. Chen, CFD-DEM simulation of flow pattern and particle velocity in a fluidized bed with wet particles, Powder Technol. 314 (2017) 346–354.
[38] C.Q. LaMarche, P. Liu, K.M. Kellogg, C.M. Hrenya, Fluidized-bed measurements of carefully-characterized, mildly-cohesive (Group A) particles, Chem. Eng. J. 310 (2017) 259–271.
[39] C.M. Boyce, A. Ozel, J. Kolehmainen, S. Sundaresan, C.A. McKnight, M. Wormsbecker, Growth and breakup of a wet agglomerate in a dry gas–solid fluidized bed, AICHE J. 63 (2017) 2520–2527.
[40] H. Xu, W. Wang, C. Ma, W. Zhong, A. Yu, Recent advances in studies of wet particle fluidization characteristics, Powder Technol. 409 (2022) 117805.
[41] H. Zhang, S. Li, DEM simulation of wet granular-fluid flows in spouted beds: numerical studies and experimental verifications, Powder Technol. 318 (2017) 337–349.
[42] T. Tang, Y. He, T. Tai, D. Wen, DEM numerical investigation of wet particle flow behaviors in multiple-spout fluidized beds, Chem. Eng. Sci. 172 (2017) 79–99.
[43] M.S. van Buijtenen, W.-J. van Dijk, N.G. Deen, J.A.M. Kuipers, T. Leadbeater, D.J. Parker, Numerical and experimental study on multiple-spout fluidized beds, Chem. Eng. Sci. 66 (2011) 2368–2376.
[44] V. Salikov, S. Heinrich, S. Antonyuk, V.S. Sutkar, N.G. Deen, J.A.M. Kuipers, Investigations on the spouting stability in a prismatic spouted bed and apparatus optimization, Adv. Powder Technol. 26 (2015) 718–733.
[45] F. Marchelli, C. Moliner, M. Curti, B. Bosio, E. Arato, CFD-DEM simulations of a continuous square-based spouted bed and evaluation of the solids residence time distribution, Powder Technol. 366 (2020) 840–858.
[46] D. Chen, X. Liu, W. Zhong, Y. Shao, B. Jin, Interactions of spout jets in a multiple-spouted bed, Can. J. Chem. Eng. 92 (2013) 1150–1159.
[47] X. Liu, W. Zhong, Y. Shao, B. Ren, B. Jin, Evaluation on the effect of conical geometry on flow behaviours in spouted beds, Can. J. Chem. Eng. 92 (2013) 768–774.
[48] X. Liu, W. Zhong, A.B. Yu, B. Xu, J. Lu, Mixing behaviors in an industrial-scale spout-fluid mixer by 3D CFD-TFM, Powder Technol. 314 (2017) 455–465.
[49] CFDEM®project, CFDEM®coupling Documentation, Version 3.X. https://www.cfdem.com/media/CFDEM/docu/CFDEMcoupling_Manual.html.
[50] C. Kloss, C. Goniva, A. Hager, S. Amberger, S. Pirker, Models, algorithms and validation for opensource DEM and CFD–DEM, Prog. Comput. Fluid Dyn. 12 (2012) 140–152.
[51] LIGGGHTS, LIGGGHTS(R)-PUBLIC Documentation, Version 3.X. https://www.cfdem.com/media/DEM/docu/Manual.html.
[52] OpenFOAM, OpenFOAM – The Open Source CFD Toolbox. https://www.openfoam.com/.
[53] R.Y. Yang, R.P. Zou, A.B. Yu, Computer simulation of the packing of fine particles, Phys. Rev. E 62 (2000) 3900–3908.
[54] Y. Gu, A. Ozel, S. Sundaresan, A modified cohesion model for CFD–DEM simulations of fluidization, Powder Technol. 296 (2016) 17–28.
[55] J.S. Marshall, S. Li, Adhesive Particle Flow, Cambridge University Press, 2014.
[56] C. Goniva, C. Kloss, N.G. Deen, J.A.M. Kuipers, S. Pirker, Influence of rolling friction on single spout fluidized bed simulation, Particuology 10 (2012) 582–591.
[57] Donald L. Koch, R.J. Hill, Inertial effects in suspension and porous-media flows, Annu. Rev. Fluid Mech. 33 (2001) 619–647.

[58] F. Marchelli, Q. Hou, B. Bosio, E. Arato, A. Yu, Comparison of different drag models in CFD-DEM simulations of spouted beds, Powder Technol. 360 (2020) 1253–1270.

[59] Z.Y. Zhou, S.B. Kuang, K.W. Chu, A.B. Yu, Discrete particle simulation of particle–fluid flow: model formulations and their applicability, J. Fluid Mech. 661 (2010) 482–510.

[60] Y. Wu, Q. Hou, A. Yu, Particle-scale study of structural transition of solid phase in gas-fluidized beds, Ind. Eng. Chem. Res. 56 (2017) 5455–5468.

[61] Y.Q. Feng, B.H. Xu, S.J. Zhang, A.B. Yu, P. Zulli, Discrete particle simulation of gas fluidization of particle mixtures, AICHE J. 50 (2004) 1713–1728.

[62] Y.Q. Feng, A.B. Yu, Microdynamic modelling and analysis of the mixing and segregation of binary mixtures of particles in gas fluidization, Chem. Eng. Sci. 62 (2007) 256–268.

[63] G.R. Chandratilleke, A.B. Yu, J. Bridgwater, K. Shinohara, A particle-scale index in the quantification of mixing of particles, AICHE J. 58 (2011) 1099–1118.

[64] M. Halidan, G.R. Chandratilleke, K. Dong, A. Yu, The effect of interparticle cohesion on powder mixing in a ribbon mixer, AICHE J. 62 (2015) 1023–1037.

[65] G.R. Chandratilleke, X. Jin, Y.S. Shen, DEM study of effects of particle size and density on mixing behaviour in a ribbon mixer, Powder Technol. 392 (2021) 93–107.

[66] D. Feng, H. Li, M. Zhu, L. Han, Y. Zhou, Insight into the interaction mechanism between liquid action and cone structure in liquid-containing gas-solid spouted fluidized bed reactors, Powder Technol. 408 (2022) 117693.